Electron Beam Induced Deposition of Platinum Contacts

Daniel Chang [a], Matthew Ervin [a], John Barry [b], Barbara Nichols [a], John Melngailis [b], Alma Wickenden [a]

[a] Sensors and Electronic Devices Directorate
U.S. Army Research Laboratory
2800 Powder Mill Road
Adelphi, MD 20783, USA

[b] Institute for Research in Electronics and Applied Physics
University of Maryland
College Park, MD 20742, USA

I. Abstract

Electron beam induced deposition (EBID) is being investigated as a means of incorporating non-conventional materials such as polymer fibers and carbon nanotubes into integrated circuits. A novel inorganic platinum precursor – $Pt(PF_3)_4$ – was tested, as it has been demonstrated to deposit Pt with conductivity close to bulk Pt. Atomic force microscopy, energy dispersive x-ray analysis, scanning electron microscopy, and other techniques were used to characterize EBID-formed Pt deposits as well as to study the mechanism of deposition. Deposit purity was shown to improve after annealing. Platinum contacts capable of integrating carbon nanotubes onto a chip were successfully demonstrated.

II. Introduction

With integrated circuits becoming ever-denser, the incorporation of non-conventional materials such as polymer fibers and carbon nanotubes could increase functionality and improve performance of future circuits. Unfortunately, traditional processes of lithography are often inapplicable or damaging to these materials or the underlying substrates. Electron beam induced deposition (EBID) is a technique that allows for local deposition of metal contacts onto a substrate with precision and control which may potentially serve the desired integrative purpose.

The process of EBID utilizes the ability of an electron beam to deposit metal from a gaseous compound known as the precursor. A tube directs the precursor gas molecules onto the substrate, where they are absorbed. A focused electron beam then causes the absorbed molecules to deposit metal by breaking the intramolecular bonds between metallic and non-metallic components. The majority of the non-metallic, residual byproducts of the precursor are desorbed and removed by the vacuum system (see figure 1 below).

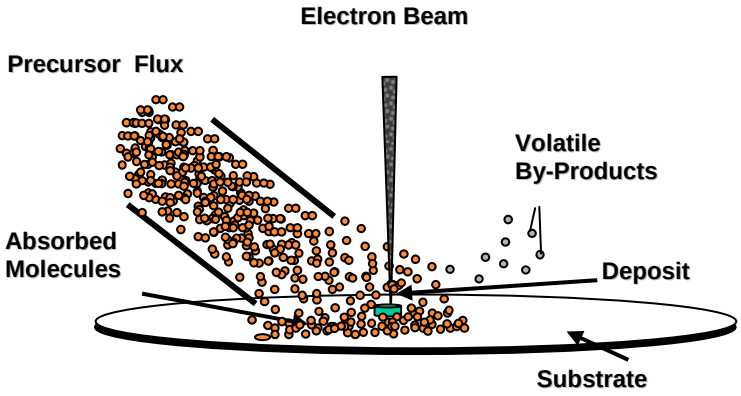

(Figure 1) Process of EBID.

EBID has marked advantages over a similar and popular deposition process known as ion beam induced deposition (IBID). Whereas ion beams can mill and damage the substrate on which deposits are formed, electron beams do not have this deleterious effect. Ion beams also use beams composed of charged ions – such as Gallium – that may result in unintended implantation; electron beams do not produce this form of contamination.

Traditionally EBID has been performed using organometallic precursors which did not yield the best metal contacts. When using organic precursors – that is, precursors containing carbon – large amounts of carbon were inevitably deposited along with the metal. [1] The carbon content increases resistivity, thus making the EBID-formed contacts conduct poorly.

Researchers at the Army Research Lab and University of Maryland have identified a novel inorganic precursor, $Pt(PF_3)_4$, that minimizes carbon contamination. Deposits have been successfully created using $Pt(PF_3)_4$. The goal of this investigation is to analyze factors that affect the qualities and physical attributes of contacts deposited using this precursor, and further to assess its usefulness in integrating non-conventional materials into integrated circuits.

III. Deposition Process

The actual deposition of platinum using EBID is a delicate process. EBID occurs within the chamber of an instrument capable of delivering a constant, focused beam of electrons. Scanning electron microscopes (SEM) were used in this research. The SEM was modified to include a $Pt(PF_3)_4$ gas injection system with a narrow, retractable gas injection tube.

The EBID procedure is similar to normal operation of an SEM, with an additional gas injection step. After the sample – that is, the substrate to be deposited on – is loaded into the SEM and the sample chamber evacuated, the desired deposition location is found using the SEM imaging and sample-manipulation capabilities. The gas injection tube is then lowered within microns of the substrate surface. However, before the precursor gas is released, the electron beam must be turned off, since platinum is deposited whenever the beam and the gas are both present. With the deposition location identified, the magnification of the SEM is adjusted to determine the deposit dimensions. For example, a 200,000x magnification yields a 1 um x 1 um deposit, and a 400,000x magnification yields 0.5 um x 0.5 um, etc.

After the deposit size and location are set, $Pt(PF_3)_4$ gas is directed onto the sample surface. The chamber pressure must be kept around $2.0 * 10^{-5}$ mBar; this is achieved through constant

monitoring and adjusting of the leak valve in the gas release system. The electron beam is turned on to start the deposition process, which is timed to provide control over deposit thickness. Examples of deposits created through this process were imaged with the SEM and depicted in figure 2 below:

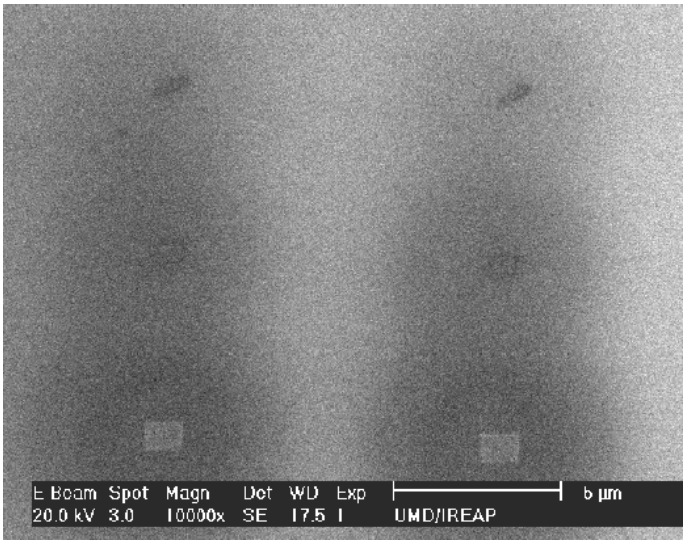

(Figure 2, above) A set of six platinum deposits, with box sizes of 0.25 um, 0.5 um, and 1.0 um

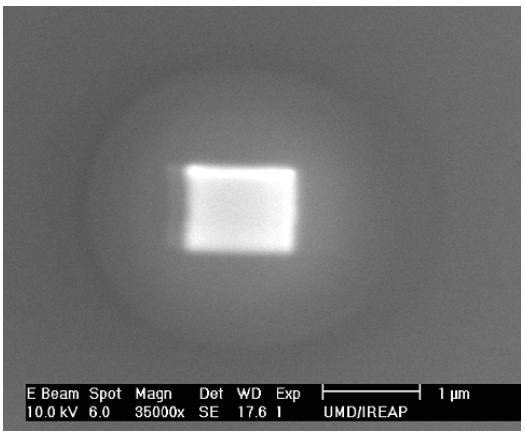

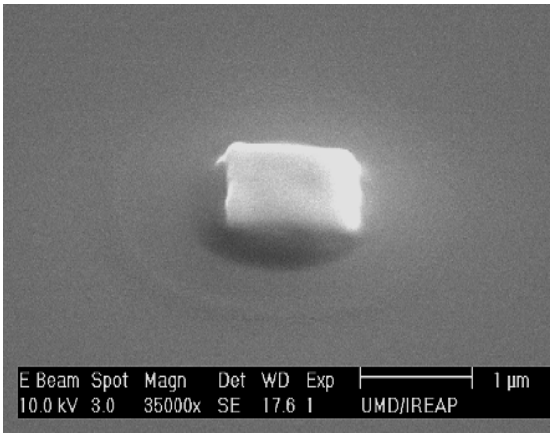

(Figure 2, above left) Image of a thick deposit, 1 um box size.
(Figure 2, above right) Image of a thick deposit tilted at 30 degrees, 1 um box size.

IV. Challenges of EBID

Although EBID using $Pt(PF_3)_4$ is promising and creates deposits successfully, there remain challenges to be addressed. The reader may have immediately noticed one such challenge in the previous figures: what are the rings around the deposits and what causes them?

This research addresses three primary challenges – which will be discussed in detail through this report – as follows:

1. Determining the mechanism of EBID that creates the aura around the central deposit.
2. Investigating whether deposit purity can be improved through annealing.
3. Demonstrating the integrative capabilities of EBID through the creation of a simple CNT circuit.

V. Challenge I: Mysterious Auras Around the Deposits

In order to be an effective means of integrating nanoscale materials into conventional circuits, EBID-created metal contacts must be precise and small. The presence of auras, as illustrated in figure 2, would undermine this purpose (see figure 3 also). The auras consume real estate and may contaminate the surrounding circuit components. Before attempting to reduce or eliminate the auras, an understanding of their formation mechanism is necessary.

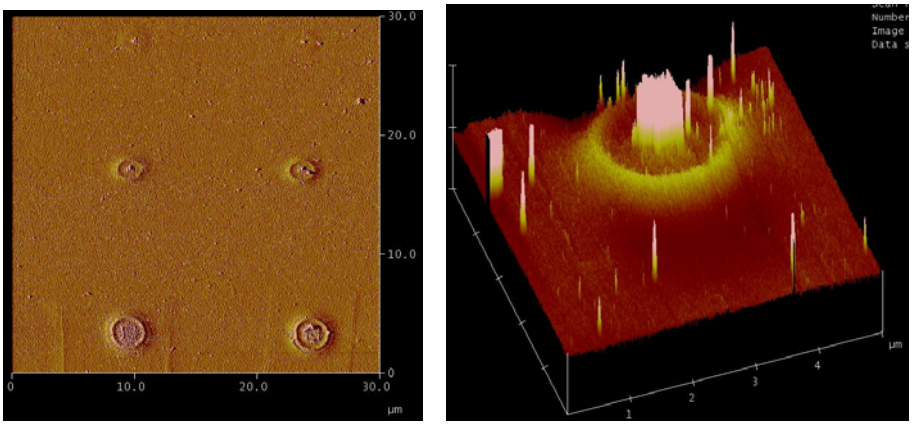

(Figure 3) Pictured here are two atomic force microscopy representations of the deposits. The image at left is a top-down representation of amplitude data; the image at right is a tilted height representation. The aura effect is easily observed in both.

V.i Approach to Understanding Aura Mechanism

It was hypothesized that the auras were created through emission of secondary electrons. Secondary emission occurs when energetic primary electrons from the electron beam excite the substrate atoms, causing them to release more electrons. These electrons may exit the substrate some distance from where the primary beam entered, react with the precursor gas, and cause the ring-shaped auras around the main deposit (see figure 4).

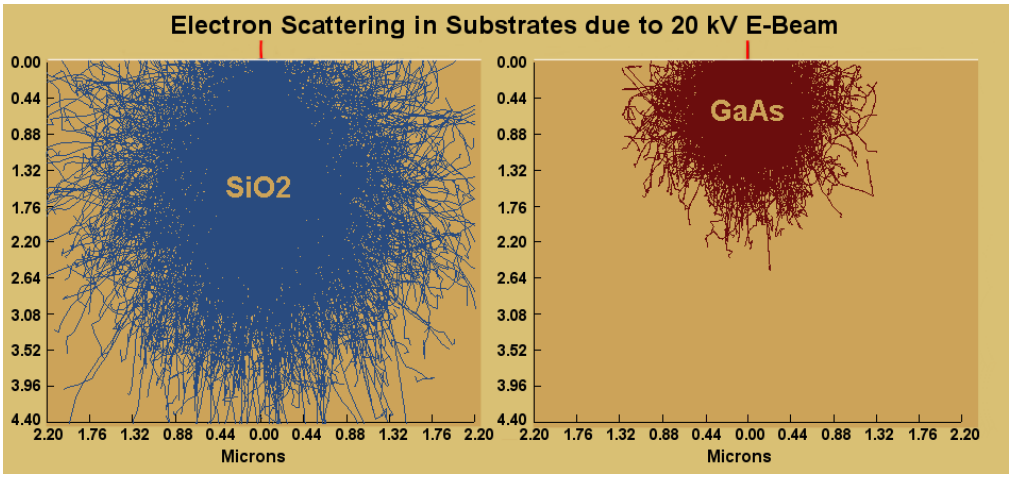

(Figure 4) Pictured here is a Monte Carlo simulation of electron scattering occurring in bulk SiO2 and GaAs samples. The red beam represents the 20 kV electron beam striking the surface, and the many scattering lines represent 2000 trajectories of simulated secondary electrons. The reemergence of electrons at the surface suggests a possible cause for the auras.

To test this hypothesis, a comparison was made between experimental and theoretical aura diameter ratios of Pt deposits made on two different substrates – SiO_2 and GaAs.

To better explain, experimental diameter ratios were found by calculating the ratio between a deposit's aura when formed on GaAs vs. a deposit's aura when formed on SiO2 under identical conditions. The sizes of the central deposits in each comparison were equal, and the deposition beam energy was set at 20 kV. Theoretical ratios were derived by extrapolating the ratio between GaAs's stopping power vs. SiO2's stopping power at 20 kV. Stopping power is a measure of the substrate's ability to bring an energized electron to a halt, and therefore how far the electron can travel within the material. Stopping power is thus used as a proxy for secondary emission

diameter size. Since secondary emission diameter depends on the substrate, a proportional correlation between experimental and theoretical diameter ratios would support the hypothesis that secondary emission causes the auras.

Deposited on each of the two substrates were a set of six 20-kV deposits, each with two 0.25 um, 0.5 um, and 1.0 um sized boxes. The doses (spot size and exposure time) were kept constant to ensure valid comparisons.

V.ii Auras: Experimental and Theoretical Data

Atomic force microscopy (AFM) was used – for its high accuracy – to analyze aura diameters, deposit heights, and provide three-dimensional images of the two experimental sets of deposits. The resultant ring diameters were found by using cross sectional analysis on the AFM utility software. The peak-to-peak distance between the cross sectional aura was used to provide the most reliable diameter measurement (see figure 5).

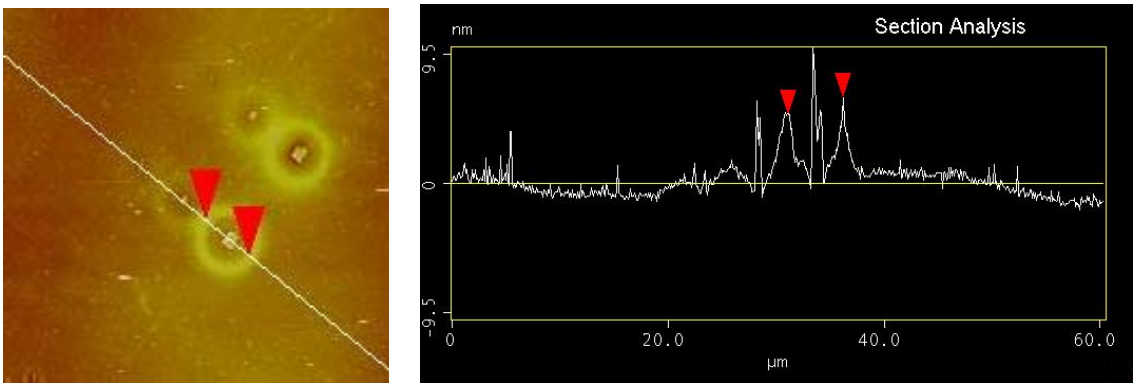

(Figure 5) AFM and Digital Instruments Nanoscope SPM v5 software were used to measure the aura dimensions. A cross-sectional white line cuts through the surface-height graph in the left image. On the right, the height and horizontal distance measurements along the line are displayed, with the red markers denoting the peaks in aura height. The tall peak surrounded by the two red markers is the desired deposit.

The experimental peak-to-peak diameter measurements and the SiO_2:GaAs diameter ratios are as follows:

	Aura diameter, SiO_2	**Aura diameter, GaAs**	**Ratio**
0.25 um box #1	3.809 um	1.410 um	2.701 : 1
0.25 um box #2	3.125 um	1.235 um	2.530 : 1
0.50 um box #1	3.812 um	1.536 um	2.482 : 1
0.50 um box #2	4.493 um	1.890 um	2.377 : 1
1.0 um box #1	5.273 um	2.526 um	2.087 : 1
1.0 um box #2	5.079 um	2.578 um	1.970 : 1

Having acquired the experimental diameter ratios, the theoretical ratios must then be found for comparison. The theoretical diameter ratio between SiO2 and GaAs at 20 kV electron beam energy was derived from experimental stopping powers of the two substrates (see figure 6). [(2)]

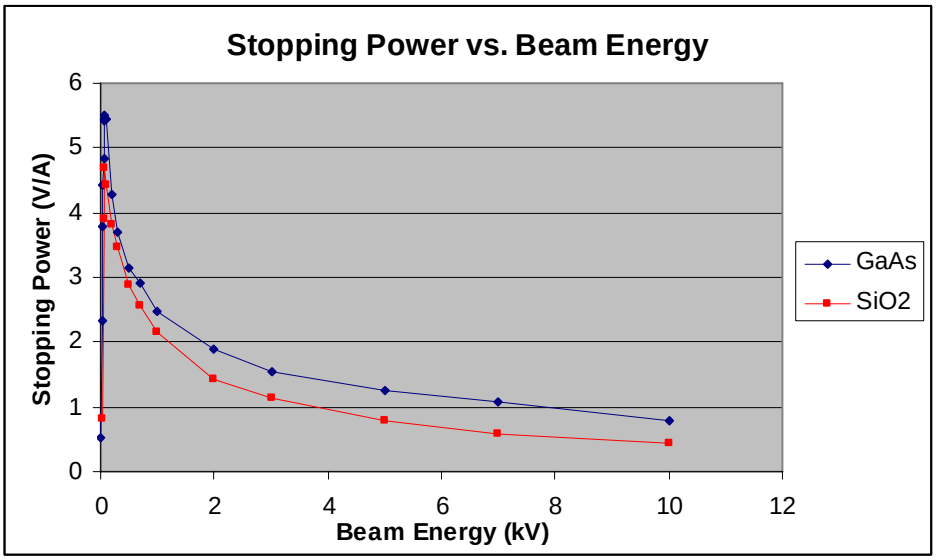

(Figure 6, above) A graph of the stopping powers of GaAs and SiO2. SiO2 has a smaller stopping power and is thus expected to have a larger aura diameter. (Figure 6, below) The ratio of GaAs:SiO2 stopping power at different energy levels. From this graph, the ratio at beam energy 20 kV is expected to be approximately 2.

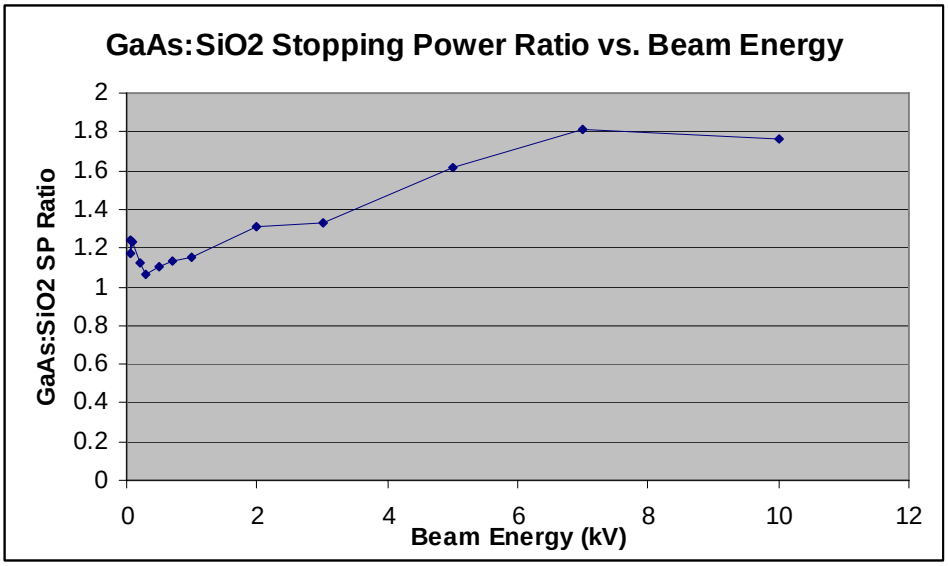

Experimental data on stopping power for GaAs and SiO2 could not be found for beam energies above 10 kV. However, as illustrated in the previous graph, the GaAs:SiO2 stopping power-ratio trend suggests that the stopping power ratio at 20 kV would be close to 2. As stopping power relates to lateral spread, the aura diameter of deposits on SiO2 should theoretically be about twice as large as for deposits on GaAs.

V.iii Auras: Results and Discussion

From the above data, the theoretical ratio between SiO2 and GaAs aura diameters should be about 2:1. The experimental ratios were indeed close to this value, with an average ratio of 2.4:1.

The Bethe range and elastic scattering can be used to explain this discrepancy. "The Bethe range is the total distance that the beam electron travels in the target while losing all of its energy. However, the Bethe range is not a good description of the maximum dimension of the interaction volume because it does not take into account the effects of elastic scattering, which cause significant deviations of the electron trajectories…[which] become significantly less than the value suggested by the Bethe range. The difference between the Bethe Range and the maximum

dimension of the interaction volume becomes greater as the atomic number of the target, and therefore the amount of elastic scattering, increases." [3]

This implies that the greater elastic scattering effect in GaAs (which has a higher density than SiO2) further shortens the actual displacement of electrons as they travel through the substrate. The actual aura diameters in GaAs, then, would be less than the expected diameter derived from stopping power alone. This may very well explain why the experimental deposit aura ratio of SiO2:GaAs is higher than the expected stopping power ratio of 2:1.

With the experimental and theoretical ratios of aura diameters on different substrates agreeing, and with the effect of elastic scattering on diameter size in mind, the results seem to imply that secondary emission is indeed the cause for the formation of the auras.

If the auras are caused by secondary emission, then two solutions may reduce aura size or eliminate them completely. The first is to lower deposition beam energy, which would greatly reduce the primary electrons' lateral straggle and therefore limit secondary electron emission to close to the impact site. The second is to deposit on thin membranes. [4] This is a mechanical way to limit the primary electron's lateral straggle since it will escape from the membrane backside before it scatters too far laterally. These two solutions to reducing the aura size may also be used as further experiments to confirm whether auras are caused by secondary emission.

Future experimentation on gas diffusion on different substrates is needed to further test the aura formation mechanism. It has been demonstrated that precursor gas molecules diffuse across the substrate surface during deposition. [5] Aura diameters may therefore be dependant on precursor molecule diffusion rates on different substrates, rather than on, or in addition to secondary emission. To clarify, the differences in aura diameters may be a function of differences in local precursor flux due to different diffusion rates on these two substrates. Future experiments making deposits at different beam energies and temperatures could distinguish between these mechanisms by altering the primary lateral straggle and diffusion rates, respectively.

VI. Effects of Annealing on Platinum Deposits

In unpublished previous experiments conducted by the team, heating EBID Pt contacted bismuth telluride nanowires improved the measured conductivity significantly. Beneficial effects of elevated temperature (during deposition) have also been found on IBID-formed copper contacts. [6] This suggests that annealing may improve the quality of EBID-formed deposits by driving off byproducts and contaminants through thermal excitation. To investigate how annealing could enhance platinum deposits, three thick deposits were formed in close proximity on the same Si substrate for annealing at varying temperatures. The deposition parameters are as follows:

	Deposit A	**Deposit B**	**Deposit C**
E-Beam Current	78 pA	579 pA	579 pA
Exposure Time	80 minutes	8 minutes	24 minutes
Deposit size	1 um x 1 um, least thick	1 um x 1 um	1 um x 1 um, thickest

VI.i Annealing: Physical Analysis of Deposits

Although chemical improvements to the deposits are the main focus of this investigation, physical effects of annealing are of interest as well and will be examined first. To perform the actual anneals, deposits were heated on a hot plate at 100^{o} C and 200^{o} C, under constant flow of nitrogen gas, for durations of 30 minutes per annealing step. SEM images of the deposits after each stage depicted as follows (see figure 7):

Sample A: Pre-Anneal **Post-100^{o} C Anneal** **Post-200^{o} C Anneal**

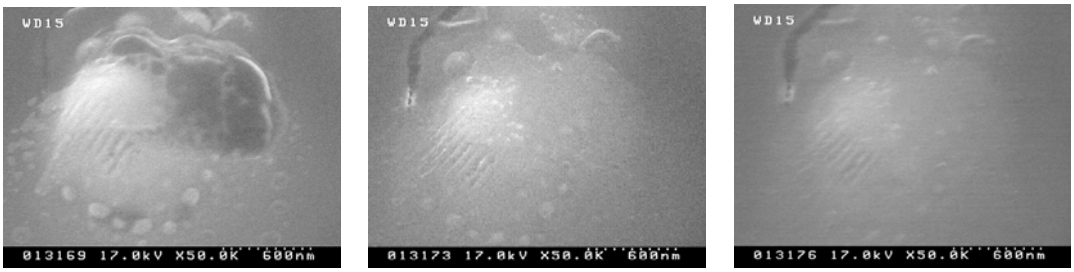

Sample B: Pre-Anneal **Post-100° C Anneal** **Post-200° C Anneal**

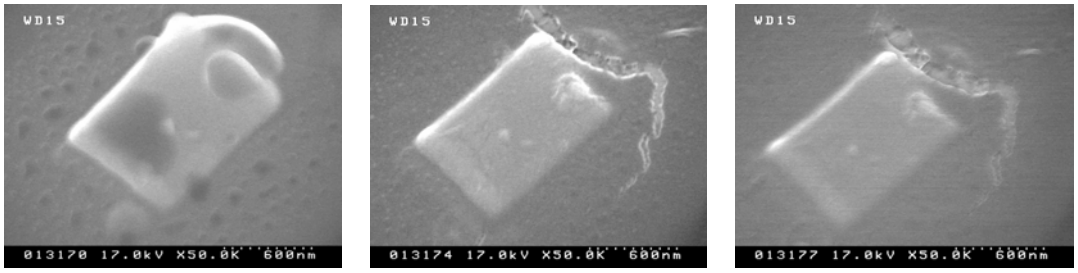

Sample C: Pre-Anneal **Post-100° C Anneal** **Post-200° C Anneal**

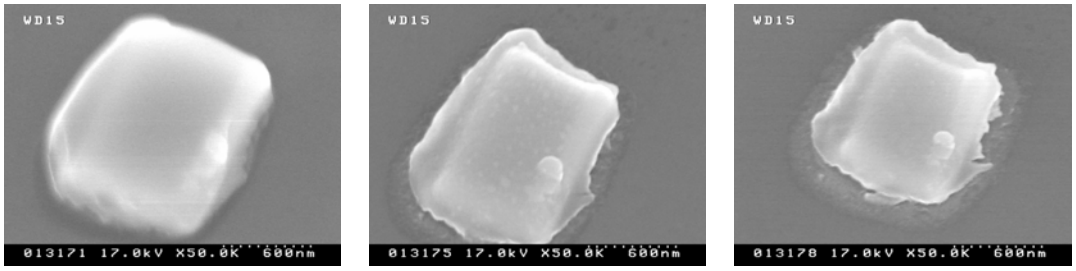

(Figure 7, above) SEM images of three deposits following each stage of annealing.

The SEM images show changes in morphology which warrant testing with more precise methods. To quantify any physical dimension changes, before-and-after AFM data was taken on another Pt deposit made on a Si substrate (see figure 8).

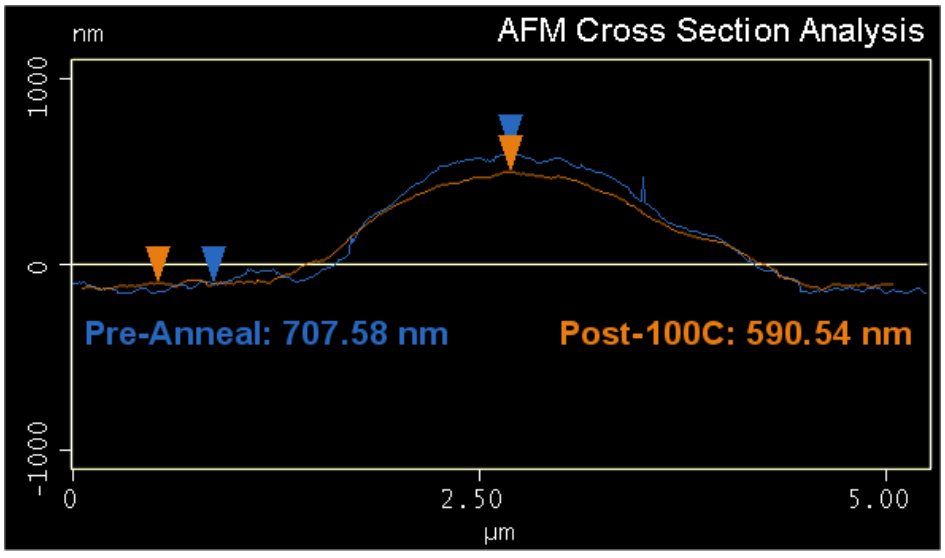

(Figure 8) AFM Cross-sectional analysis of Pt deposit before and after annealing.

There is very little noticeable change in deposit width following a 100° C anneal. However, the height dropped by 16%.

VI.ii Annealing: Chemical Analysis of Deposits

Energy dispersive x-ray analysis (EDX) evaluates the elemental makeup of a material. Each element has peaks at characteristic energies, with atomic concentrations related to the peak area.

The chemical composition of the deposits were taken using EDX for pre-anneal (25^{o} C), post-100^{o} C anneal, and post-200^{o} C anneal stages. Theoretically, annealing could drive off volatile fluorine- and phosphorous-containing contaminants that were incorporated during the EBID deposition, thus reducing impurities and improving contact quality.

VI.iii Annealing: Results and Discussion

The compositions of possible major contaminants – phosphorous and fluorine – were traced after each stage of annealing for all samples A through C. The results of each EDX spectrum were normalized with respect to the Pt-L peak of one spectrum to ensure valid comparisons.

Surprisingly, the EDX readings for fluorine were negligible for all samples, and thus excluded in this report.

Unfortunately, the phosphorous peak is unresolved from the Pt-M peak. To infer the content of phosphorous, the spectra were normalized to the platinum-L peak to ensure a constant Pt contribution to the P peak. The changes in the platinum-phosphorous shared peak then suggested changes in phosphorous content. Due to the P/Pt peak convolution, comparisons cannot be made between different samples which will have different Pt peak ratios for reasons outside of the scope of this paper. The results of the EDX analyses are as follows (see figure 9):

Phosphorous Composition (units in peak-counts per second):

	Pre-Anneal	**100^{o} C Anneal**	**200^{o} C Anneal**
Deposit A	2931	2577	2446
Deposit B	2848	2415	2119
Deposit C	3253	2848	2923

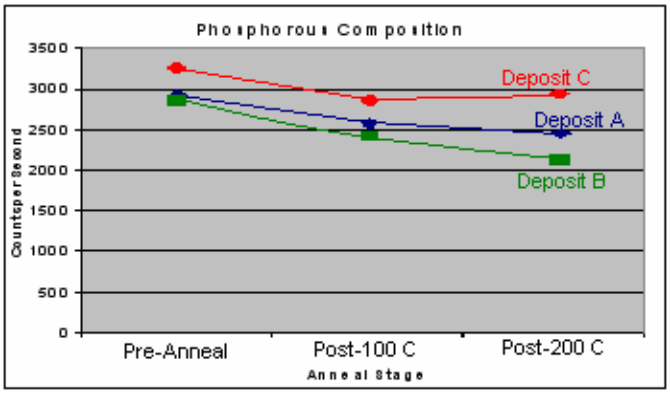

(Figure 9, above) Graph exhibiting decreasing P content following annealing in all three samples.

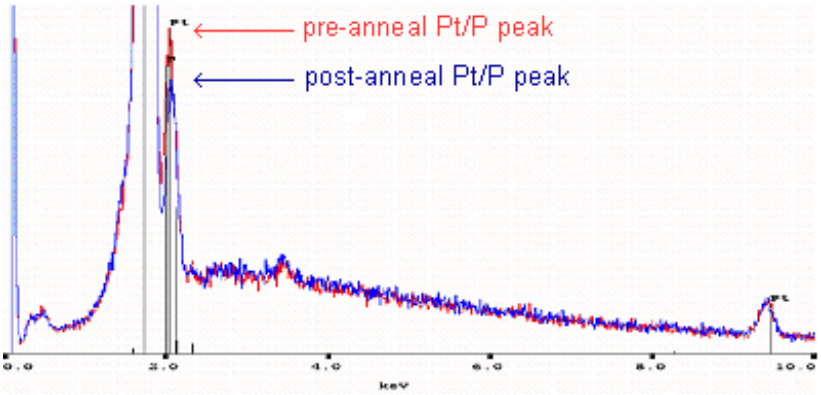

(Figure 9, above) EDX spectra for Deposit A. Red spectrum is pre-anneal and has a taller Pt/P peak. Blue spectrum is post-200 C anneal and has a reduced P content.
Both spectra were normalized to the right-most pure Pt peak for comparison.

The data indicates that annealing the platinum deposits decreases phosphorous contamination. The physical dropping in height and the reduction of phosphorous content appear to indicate that the deposits are being purified during the low temperature annealing, thus improving in quality. The results are promising, as annealing has reduced the largest impurity in the platinum contacts. The ease with which byproduct contaminants can be removed from deposits – simply through light heating – reinforces the value of $Pt(PF_3)_4$ in creating quality contacts for device integration.

This experiment analyzed how contacts can be improved with post-deposition annealing. Another worthwhile experiment for the future would be to examine the conductivity improvements after annealing or deposition at elevated temperatures.

VII. Integrative Capabilities of EBID: Carbon Nanotube Circuit

While the aura mechanism and deposit qualities have been studied, the focus of this research is to demonstrate the ability of EBID to integrate nanoscale materials into conventional circuits. Integrating a carbon nanotube (CNT) onto a simple circuit defined by two gold contacts would be a good example of EBID's integrative capabilities.

VII.i CNT Circuit: Method

The idea was to transplant and attach (using EBID) a CNT to a simple circuit. Single-walled carbon nanotubes (CNTs) were grown across trenches on a substrate. CNTs are a few nanometers across, therefore scanning electron microscopy and a Zyvex Nanomanipulation system were used to cut and move them.

The Zyvex has four probe tips, each approximately 200 nm wide at the tip. Two pairs of two tips were moved to touch each end of the CNT, which was still suspended across the trench and attached to the substrate. Current was passed between two adjacent probe tips to overload and thus cut the CNT at one end. Intermolecular forces kept the severed CNT attached to the probe tips. The same process was repeated with the second pair of probes on the other end of the CNT, until the CNT was cut on both ends and attached between two probes (see figure 10).

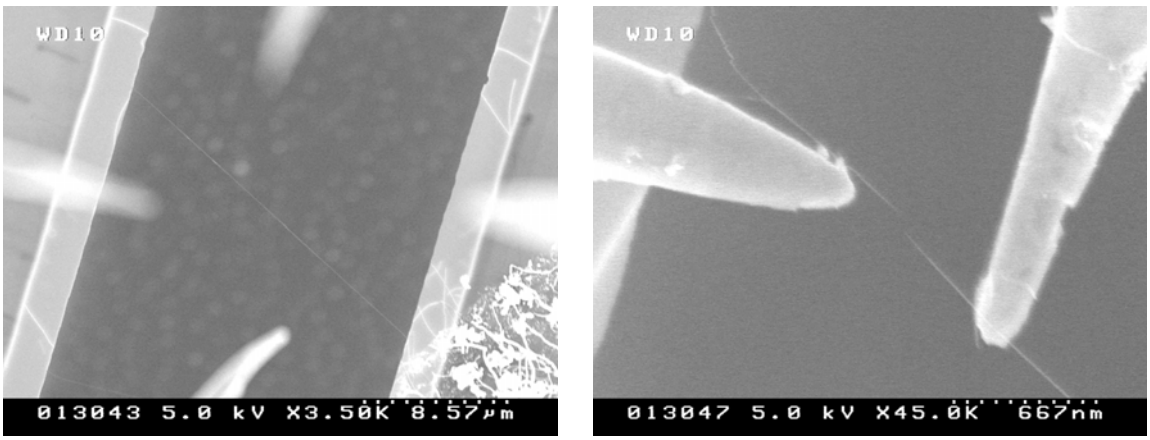

(Figure 10, above left) The four Zyvex probes hover above the CNT, in preparation for transplantation. (Figure 10, above right) A pair of two probes connect to one end of the CNT and cut it by passing current. Intermolecular forces keep the CNT connected to the probes after it is cut.

The two probes, now holding the CNT, were then moved above two gold contacts on another SiO2 substrate, and lowered to the surface until the CNT bridged the gold contacts. Because intermolecular forces still hold the CNT to the probe tips, carbon contamination (a usually undesired form of EBID using the residual organics in the SEM) was used to pin the CNT down to the gold contacts, and the Zyvex probes were removed.

Finally, EBID was used to deposit Pt on each end of the CNT. The Pt deposits provided mechanical and electrical contact, integrating the CNT into the simple circuit comprising two gold contacts (see figure 11).

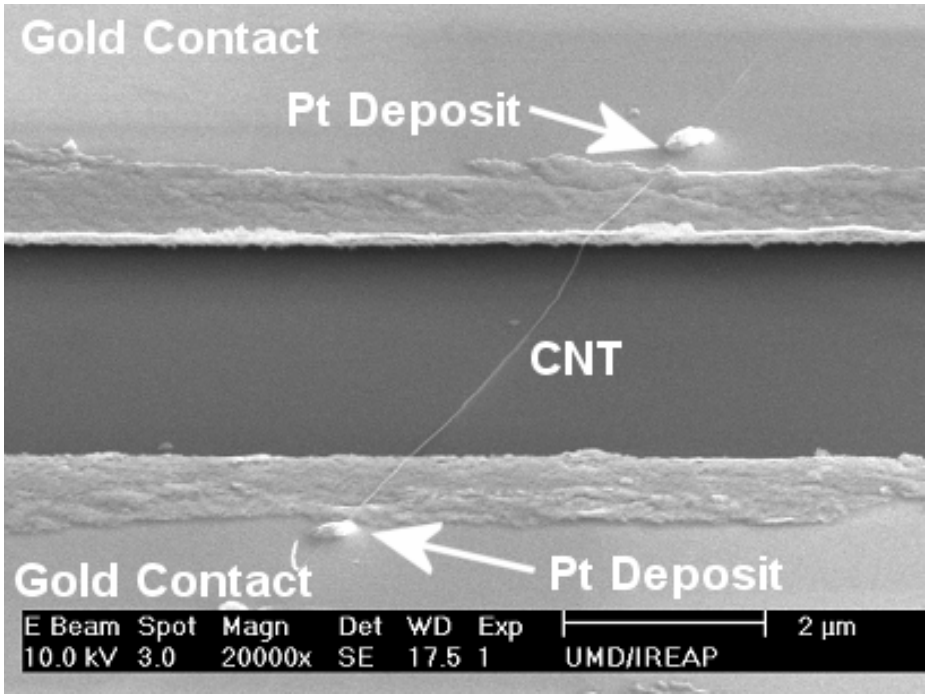

(Figure 11) SEM image of the completed CNT circuit.

VII.ii CNT Circuit: Results and Discussion

The CNT circuit successfully passed current, and resistance measurements were taken. Low temperature annealing on the circuit resulted in lower resistance measurements, with a pre-anneal resistance of ~520 kOhm and a post-100^{o} C resistance of ~290 kOhm – a 44% improvement. This confirms again the beneficial effect of low temperature annealing on contact quality.

After several resistance measurements, the CNT broke due to current overflow (see figure 12). The snap in the CNT was not desired, but it verifies that the current was passing through the CNT which attests to the ability of EBID-formed Pt contacts to apply successful mechanical and electrical contact in order to integrate the CNT into the circuit.

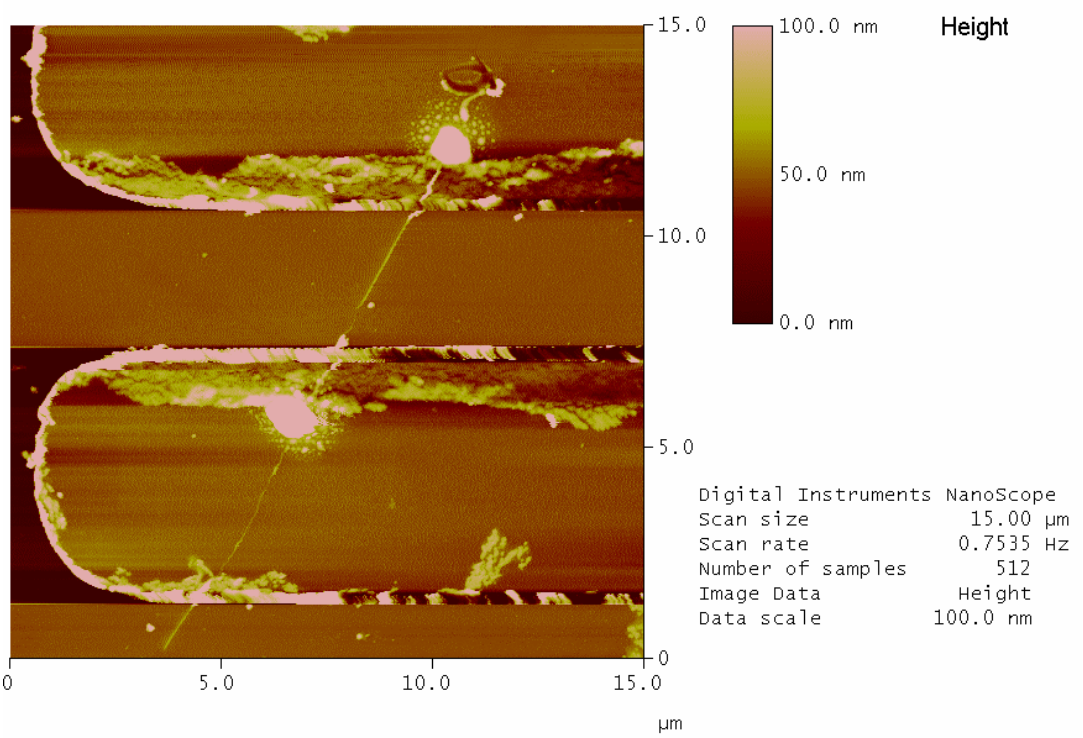

(Figure 12) Atomic force microscopy image of broken CNT circuit.
Notice the cut in the CNT near the lower gold contact.

This successful demonstration showcases EBID's capability of integrating nanoscale materials into a circuit, and should promote interest in the EBID process. Future work might include building more complex devices, such as a CNT field effect transistor, or polymer fiber sensors.

VIII. Conclusion

Electron beam induced deposition with the novel inorganic $Pt(PF_3)_4$ precursor was investigated as a means of incorporating nanoscale materials into circuits.

The main limitation of EBID appears to be the auras that form around the central deposits. The tests conducted in this research suggest secondary emission to be the aura-formation mechanism. This may imply that auras can be reduced or eliminated by using lower deposition beam energies, or depositing on thin membranes.

Further investigations have shown that the Pt deposits improve in chemical purity following low-temperature annealing. The CNT circuit resistance dropped 44% following annealing as well, suggesting low-temperature annealing to be significantly beneficial in improving contact quality.

From the experimental results, EBID deposition of platinum contacts from the $Pt(PF_3)_4$ precursor appears to be a promising method of integrating nanoscale materials. The successful demonstration of a simple CNT circuit attests to this potential. Creating complex devices with EBID should be attempted to further confirm these abilities.

IX. Acknowledgements

I would like to thank the University of Maryland's MERIT program and the Army Research Lab for providing me with this unique research opportunity. I would especially like to thank Matthew Ervin for his guidance and insightful explanations of the science behind EBID and nanotechnology. Thanks also to John Barry for spending many hours helping me make deposits, and Barbara Nichols for teaching me how to run the AFM. Finally, I would like to thank John Melngailis and Alma Wickenden for explaining concepts of the research and helping me form ideas for my research focus.

X. References

(1) J. Melngailis. SPIE Vol. 1465. p. 36, 1991

(2) D. C. Joy, A Database of Electron Solid-Interactions, 2004. http://pciserver.bio.utk.edu/metrology/download/E-solid/database.doc (viewed 8/7/2006)

(3) Joseph I. Goldstein, Dale E. Newbury, Patrick Echlin, David C. Joy, A.D. Romig, Jr., Charles E. Lyman, Charles Fiori, and Eric Lifshin. Page 88, Scanning Electron Microscopy and X-Ray Microanalysis, Second Ed. Plenum Press, 1992, New York.

(4) van Dorp WB, Hagen CW, van Someren B, Kruit P, Crozier PA: Approach to resolution limit of nanometer scale electron beam induced deposition. *Nanoletters 5*, 1303-1307 (2005)

(5) S. Haraichi, M. Komuro. Jpn. J. Appl. Phys. Vol 32 (1993) pp. 6168-6172.

(6) A. D. Della Ratta, J. Melngailis, C. V. Thompson. J. Vac. Sci. Technol. B 11(6), Bov/Dec 1993.